RESEARCH ARTICLE | MAY 16 2023

Intense widely controlled terahertz radiation from laser-driven wires

N. Bukharskii ; Ph. Korneev

Matter Radiat. Extremes 8, 044401 (2023)
https://doi.org/10.1063/5.0142083

Matter and Radiation at Extremes

RESEARCH ARTICLE

scitation.org/journal/mre

Intense widely controlled terahertz radiation from laser-driven wires

Cite as: Matter Radiat. Extremes 8, 044401 (2023); doi: 10.1063/5.0142083
Submitted: 11 January 2023 • Accepted: 22 April 2023 •
Published Online: 16 May 2023

N. Bukharskii[a] and Ph. Korneev[b]

AFFILIATIONS

National Research Nuclear University MEPhI, 31 Kashirskoe shosse, 115409 Moscow, Russian Federation

[a]**Author to whom correspondence should be addressed:** n.bukharskii@gmail.com.
Also at: P. N. Lebedev Physical Institute of RAS, 53 Leninskii Prospekt, 119991 Moscow, Russian Federation.
[b]**Electronic mail:** ph.korneev@gmail.com. **Also at:** P. N. Lebedev Physical Institute of RAS,
53 Leninskii Prospekt, 119991 Moscow, Russian Federation.

ABSTRACT

Irradiation of a thin metallic wire with an intense femtosecond laser pulse creates a strong discharge wave that travels as a narrow pulse along the wire surface. This traveling discharge efficiently emits secondary radiation with spectral characteristics that are mostly defined by the wire geometry. Several examples of designs are considered here in the context of generation of intense terahertz radiation with controllable characteristics for various scientific and technological applications. The proposed setup may be easily realized, and it has the merits of robustness, versatility, and high conversion efficiency (reaching several percent) of laser energy to terahertz radiation.

I. INTRODUCTION

Much research in recent years has been devoted to the development of technology for generating terahertz (THz) radiation, i.e., electromagnetic radiation with frequencies between 100 GHz and 10–30 THz.[1–3] The ever-increasing attention paid to this topic stems from numerous possible applications of THz radiation in both fundamental science and technology. Many of these applications belong to biological and medical science, which is not surprising considering the unique properties of THz waves. Unlike x-rays, they do not cause harm to biological tissues, since THz frequencies are too low to ionize biomolecules, and, at the same time, many vibrational, rotational, and oscillating molecular degrees of freedom are excited in the THz range. These factors, along with its lower scattering loss in biological tissues in comparison with infrared or visible light, make THz radiation an ideal candidate for medical imaging and spectroscopy of biological objects.[4,5] One area of particular interest here is cancer detection and treatment with THz radiation.[6–11] In this case, THz waves may be used to detect and manipulate a molecular resonance of cancer DNA, which can be observed at about 1.65 THz and occurs due to chemical and structural alterations that biomolecules undergo in cancer cells.[12–15] THz imaging can also be applied more widely, for example, in security-related applications.[16,17] Owing to the high penetration of THz radiation into dry, nonmetallic, and nonpolar materials, it can be used to image individual internal regions where the absorption is high, such as areas with water content,[18] or it can help to identify the distribution of defects in materials with low absorption, such as foams.[19] Another potential field of application for THz radiation is related to the study and manipulation of material properties. In contrast to visible light, its photons do not carry excessive energy, allowing for the direct coupling into excitation states of interest and opening pathways for a vast range of perspective studies.[20] Finally, it is worth mentioning the possibility of using THz radiation for increasing the bandwidth of wireless communications systems, enabling faster transmission of a larger amount of data.[21,22] All these applications require a certain amount of spectral control, and many of them demand high intensity levels.

Various techniques for generating THz radiation have been developed. Among these are photoconductive antennas, optical rectification, and laser–plasma interaction schemes, as well as a number of methods based on topological insulators, spintronic materials, and metasurfaces.[23] In the context of high achievable intensities, methods involving relativistic laser-produced plasmas may be preferable, since the output from laser plasmas does not experience saturation up to very high intensities and there is no

risk of damaging the active radiating medium.[24] One of the widely considered approaches to generate powerful THz radiation has been developed in a number of recent numerical and experimental studies[25–33] and uses straight laser-driven metallic wires. With these, fast laser-accelerated electrons perform collective motion leading to a coherent emission of electromagnetic waves. However, the creation of fast electrons with a short laser pulse also results in a fast, powerful, and compact discharge current,[34–36] which may appear to be even more suitable for THz emission, being under some conditions more strong and coherent, as in the case discussed in Ref. 37, where the resulting magnetic field was determined by the discharge current rather than the current of accelerated electrons. In this work, we show that modification of the wire geometry by shaping it as a curved periodic structure presents wide possibilities for control of the generated radiation emitted by such discharge pulses. Some benefits of using discharge pulses in this context were recently discussed in Ref. 35 for the case of a coil-shaped wire. However, in that case, certain specific conditions are needed to achieve a high efficiency, which may cause practical difficulties. In the present work, it is shown that the use of an extended undulatory wire as a THz antenna possesses both robustness and simplicity, provides excellent control, and allows for the generation of very high intensity THz radiation with very high efficiency. We demonstrate this, considering three types of wire profiles, namely, sinusoidal (hereinafter simply "sine"), triangle-shaped, and square-shaped (hereinafter simply "triangle" and "square," respectively) targets, irradiated by an intense femtosecond pulse on one of the open ends; see Fig. 1.

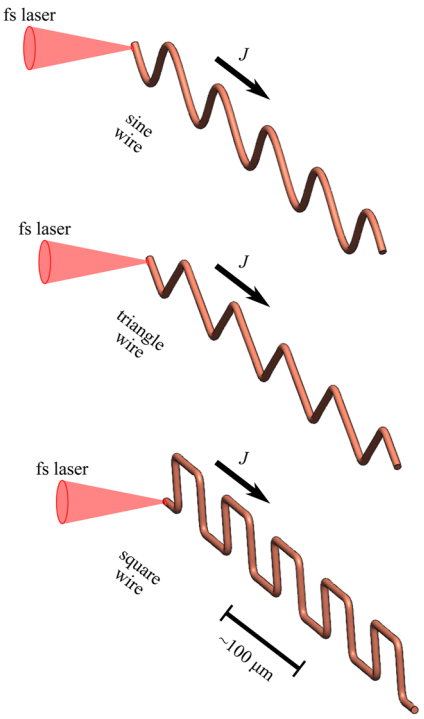

FIG. 1. Sketch of the proposed targets: "sine" wire (top), "triangle" wire (middle), and "square" wire (bottom). The targets are irradiated at the open end by an intense femtosecond laser pulse. The general propagation direction of the laser-induced discharge pulse is shown by black arrows: it propagates from the irradiated end of the wire to the opposite one along the wire surface.

II. DISCHARGE PULSE FORMATION AND SCALINGS

The amplitude of the discharge pulse and its duration depend on the laser pulse parameters. For this setup, short laser pulses are required, i.e., those with a duration τ that is short compared with L/c (see the related discussion in Ref. 38), where c is the velocity of light and L is a characteristic size of the target (e.g., its length). As is demonstrated below, the expected discharge pulse duration is similar to the laser pulse duration, and the discharge pulse intensity is proportional to the laser pulse intensity, assuming the interaction conditions to be the same. To obtain a more detailed description of the process of discharge pulse formation, it was studied numerically with the particle-in-cell (PIC) code Smilei.[39] Simulations were performed in a reduced 2D setup with a simple straight wire target. This simple setup allows the process of the discharge pulse formation and propagation to be studied for various parameters of the laser driver. For all the simulations that were performed, the target presented a $40 \times 1\ \mu m^2$ rectangle positioned at the center of the $48.7 \times 12.2\ \mu m^2$ simulation box, which contained 3072×768 cells. The size of one cell in both dimensions was ~15.9 nm, with ten particles of each kind per cell, and the time resolution was 1.8×10^{-2} fs. The target consisted of ions with atomic number $Z = 79$, which corresponds to gold, with mass $M = 5 \times 10^3 m_p$, where m_p is the mass of a proton. Although the ions would not noticeably move on the time scale considered, their mass was increased to provide qualitatively the same ion dynamics as in the case of a target of more realistic size about five to ten times greater than the size of the target in this parametric study. The density of ions at the start of the simulation was set to $n_i = 5.9 \times 10^{22}\ cm^{-3}$, which is the solid-state ion density for gold. Initially, the degree of ionization of the target as well as its electron density were set to zero, and the field ionization model implemented in Smilei was employed to calculate the values of the aforementioned parameters on each step. The laser pulse was introduced into the simulation box from the lower edge of the box and irradiated the target at an angle of 45° to its surface. This angle was chosen for better absorption of the laser energy as the laser pulse propagated some distance along the target together with the induced discharge wave. Three different laser pulse durations were considered: $\tau_{las.} = [12.5, 25, 50]$ fs, with the given values corresponding to the full width at half maximum (FWHM) size of the temporal profile. For each duration, five different values of maximum intensity in focus were taken: $I_{max} = [2 \times 10^{19}, 10^{20}, 10^{21}, 10^{22}, 10^{23}]\ W/cm^2$.

The results of one of the performed simulations (with $I_{max} = 10^{22}\ W/cm^2$ and $\tau_{las.} = 12.5$ fs) are presented in Figs. 2(a1)–2(a4). From the plots of the B_z component of the electromagnetic field, one can see that the laser irradiates the wire on the left end; see Fig. 2(a1). The laser pulse is then partially reflected and partially absorbed by the target; see Fig. 2(a2). A substantial part of the laser energy is converted into the energy of a discharge pulse that continues to propagate autonomously along the wire to the right, in the direction of its opposite end, even when most of the laser pulse leaves the simulation box; see Figs. 2(a3) and

2(a4). The excited discharge wave is monopolar, which is consistent with the results obtained in other works; see, e.g., Refs. 32, 34, and 40. For the ultrashort laser drivers considered in this study, the wave is localized well on the scale of the wire, i.e., it has the form of a distinct short electromagnetic pulse. The amplitude of the discharge current pulse and its duration at FWHM $\tau_{d.p.}$ depend on the parameters of the laser driver. The results of the parametric scan that was performed are summarized in Figs. 2(b) and 2(c).

As can be seen in Fig. 2(b), the dependence of the amplitude of the discharge current J_0 for all the laser durations considered appears

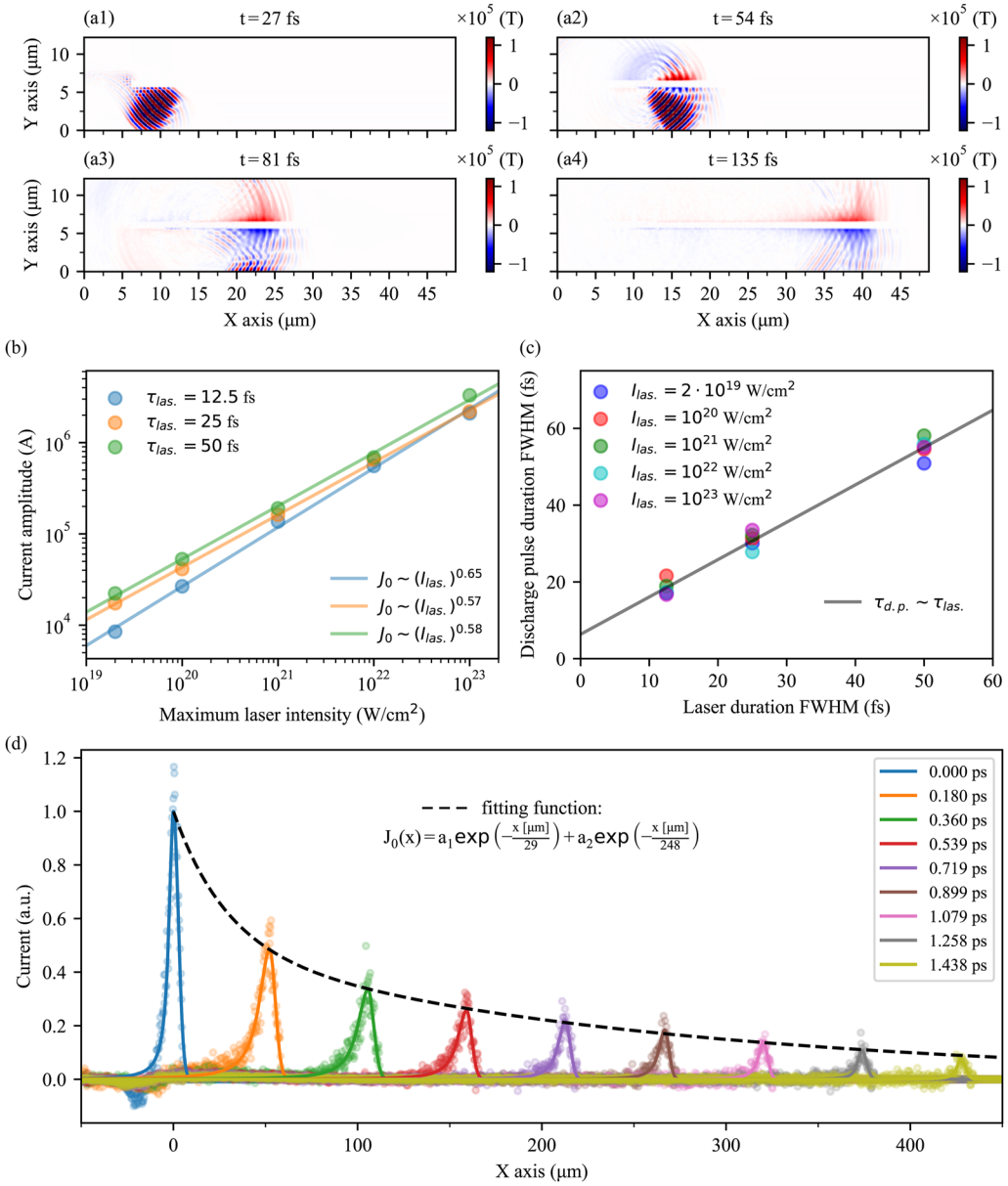

FIG. 2. (a1)–(a4) Results of 2D PIC simulation for a straight wire target irradiated by a laser pulse with maximum intensity $I_{max} = 10^{22}$ W/cm^2 and FWHM duration $\tau_{las.} = 12.5$ fs: B_z component of the electromagnetic field at moments of time 27, 54, 81, and 135 fs, respectively. (b) Dependence of the amplitude of the total electric current flowing through the wire cross-section at $x \approx 30$ μm on the maximum laser intensity at the focal spot; the data for different laser pulse durations are shown by markers of different colors. The points appear to closely follow the power laws represented by solid lines. (c) Dependence of the duration of the discharge pulse at FWHM on the laser duration at FWHM for various intensities of the laser driver, shown by markers of different colors. The points appear to closely follow the linear dependence represented by the black solid line. (d) Evolution of the current profile as it propagates along the wire. The dashed line shows an approximation by the sum of two exponential functions.

to closely follow the power-law dependence $J_0 \sim (I_{las.})^k$, with $k \approx 0.6 \pm 0.05$. In the simplest consideration, the expected value of k is 0.5, since the magnetic and electric field amplitudes depend linearly on the current and are proportional to the squares of the magnetic and electric field energy densities, which in turn are directly proportional to the laser energy and consequently its intensity. The result obtained here, however, suggests that the laser-to-discharge-pulse conversion efficiency is somewhat higher than expected, which can be explained by the reduced effects of processes of dissipation such as ionization at high laser intensities. Comparison of the results for different laser pulse durations also shows that the current amplitude increases with increasing laser duration, although the differences are more pronounced at low intensities. This behavior may be attributed to the higher laser energy delivered to the target when the laser pulse duration increases with its intensity remaining constant. As Fig. 2(c) shows, the duration of the discharge pulse depends almost linearly on the duration of the laser pulse, implying that the former can be directly controlled by adjusting the latter. The propagation velocity of the discharge pulse in the range of parameters considered shows no dependence on the intensity or the laser driver duration and is ~0.97c–0.98c.

Another important question is the evolution of the discharge current during its propagation along the extended wire targets. To estimate the effects of dispersion and energy dissipation, an additional simulation for a long straight wire target of length ~500 μm was performed, with the other parameters being the same as before. A laser pulse with an intensity of $\sim 4 \times 10^{21}$ W/cm^2 and a duration at FWHM of ~25 fs was focused at an angle of 45° to the target surface into a focal spot of diameter 4 μm. The extracted electric current profiles at different moments of time are presented in Fig. 2(d). The discharge current pulse has an initial sharp rise, which is similar to the temporal shape of the intensity envelope of the laser pulse, and a somewhat longer trailing edge with a pronounced tail that resembles a Lorentzian function. This shape is preserved well as the current pulse propagates to the right along the wire. The results obtained indicate that dispersion does not play a significant role at propagation distances of ~500 μm, whereas energy dissipation is noticeable. The decay of the current amplitude may be fitted with a sum of two exponential functions with different characteristic decay scales. In the first stage, after formation of the discharge pulse at $x = 0$ μm, the amplitude decreases rapidly with a characteristic decay scale of ~30 μm, but, later, the decay rate reduces to that of a characteristic scale of ~250 μm. For some targets, such as the examples considered here, the latter value is of the same order as the target period, defining the radiation spectra. In this situation, the energy dissipation may result in the imposition of a slowly varying envelope on the emitted electromagnetic field profiles and the addition of corresponding frequencies to the spectra; see Fig. 5(a) below.

It should be noted that in at least one detailed experimental study of discharge propagation,[36] although this was performed for longer laser pulses of ~500 fs and higher energies of ~50 J, no noticeable dissipation was reported on the scale of a few millimeters. It may be expected that the artificially reduced small wire thickness in the simulations results in stronger absorption of the discharge pulse energy, since the surface fields in the propagating electromagnetic wave scale as ~$1/r$ with the radius of the wire.[36] For the lower discharge pulse absorption anticipated for real-size targets, the efficiency of the THz radiation generation may considerably increase, and further theoretical and experimental studies are necessary to clarify this point.

The numerical modeling performed here indicates that the discharge pulses are formed in a broad range of laser intensities, with the parameters of the induced discharge pulses being determined by the parameters of the laser driver, and almost without an initial width change. As was confirmed in special simulations, for shaped wires the discharge pulse formation and propagation occur in the same way as they do for the straight wire targets. However, in shaped targets, the discharge pulse propagates along the target following its geometry, and, according to the subsequent analysis detailed below, when such discharge pulses are propagating along an extended curved wire, they may radiate powerful THz waves with properties defined by the wire geometry.

III. GENERATION OF THZ RADIATION IN UNDULATING WIRE TARGETS

Consider the emission of radiation for a discharge pulse propagating along a given shaped wire. First, to illustrate the great variety and geometrical control of the generated radiation, three types of targets were considered in the numerical simulations: "sine" (Fig. 1, top), "triangle" (Fig. 1, middle), and "square" (Fig. 1, bottom). The electric current had the longitudinal spatial profile obtained in the simulations described in Sec. II, with a sharply rising front and a trailing edge with a pronounced tail [see Fig. 2(d)], but without dissipation being taken into account, since, on the one hand, this question needs clarification as discussed above, and, on the other hand, it would hinder understanding of the profiles, which are shown in arbitrary units. This current pulse was spatially shaped and propagated along the wire of given geometry. The current was considered to be uniform in the transverse cross-section of the wire. Although the results of the simulations with plasma [see Fig. 2(a)] show that the fields do not penetrate into the wire, and so the currents flow on the surface, we verified that this simplification does not change the emitted field profiles far from the wire in the wave zone, on a spatial scale where the current distribution is not important provided its localization is smaller than the radiation wavelength. The amplitudes of the fields excited by the propagating discharge current depend linearly on its amplitude, and they can then be rescaled to a given intensity of the laser driver in accordance with the power law derived from the numerical parametric simulations in Sec. II; see Fig. 2(b).

Although in our simulations with straight wire targets, the propagation velocity appears to be ~0.97c–0.98c, there are some experimental data with lower values down to about 0.8c; see, e.g., Ref. 36. So, we consider the propagation velocity here as a free parameter, which may only quantitatively change some results; for all simulations in this section, the propagation velocity was set to $v_0 = 0.9c$. Radiation was calculated with the Yee 3D Maxwell solver implemented in Smilei.[39] The cell size was $2.5 \times 2.5 \times 2.5$ μm^3, which is adequate in this modeling where small-scale plasma dynamics are not taken into account. The simulation box consisted of $512 \times 512 \times 512$ cells and had dimensions $L_x \times L_y \times L_z$ of

$1.28 \times 1.28 \times 1.28\ \text{mm}^3$. This is much greater than the characteristic target size ~100 μm and is sufficient to study electromagnetic waves emitted from the target in the wave zone.

The "sine" wire target geometry was defined as follows:

$$\begin{cases} y = L_y/2 + a\,\sin(x/a), \\ z = L_z/2, \end{cases} \tag{1}$$

where $x \in [0.05, 1.23]$ mm, and $a \approx 20$ μm defines the characteristic scale of the target and the length of one period of the wire. The wire had a circular cross-section, 5 μm in diameter. This value is a few times greater than that used in the numerical modeling discussed in Sec. II, but is still much smaller than the emitted wavelength, defined mainly by the wire undulation period as shown below. For thicker targets, which may be more easily manufactured, the results obtained here remain valid unless the wire thickness becomes comparable to the undulation period. For even thicker targets, the problem needs to be reconsidered, but the radiation would not disappear, since it would not disappear for a semi-infinite target with an undulating structure on the surface. However, it should be noted that the wire diameter may play a role if one excites a helical discharge propagation, which may become possible when the laser

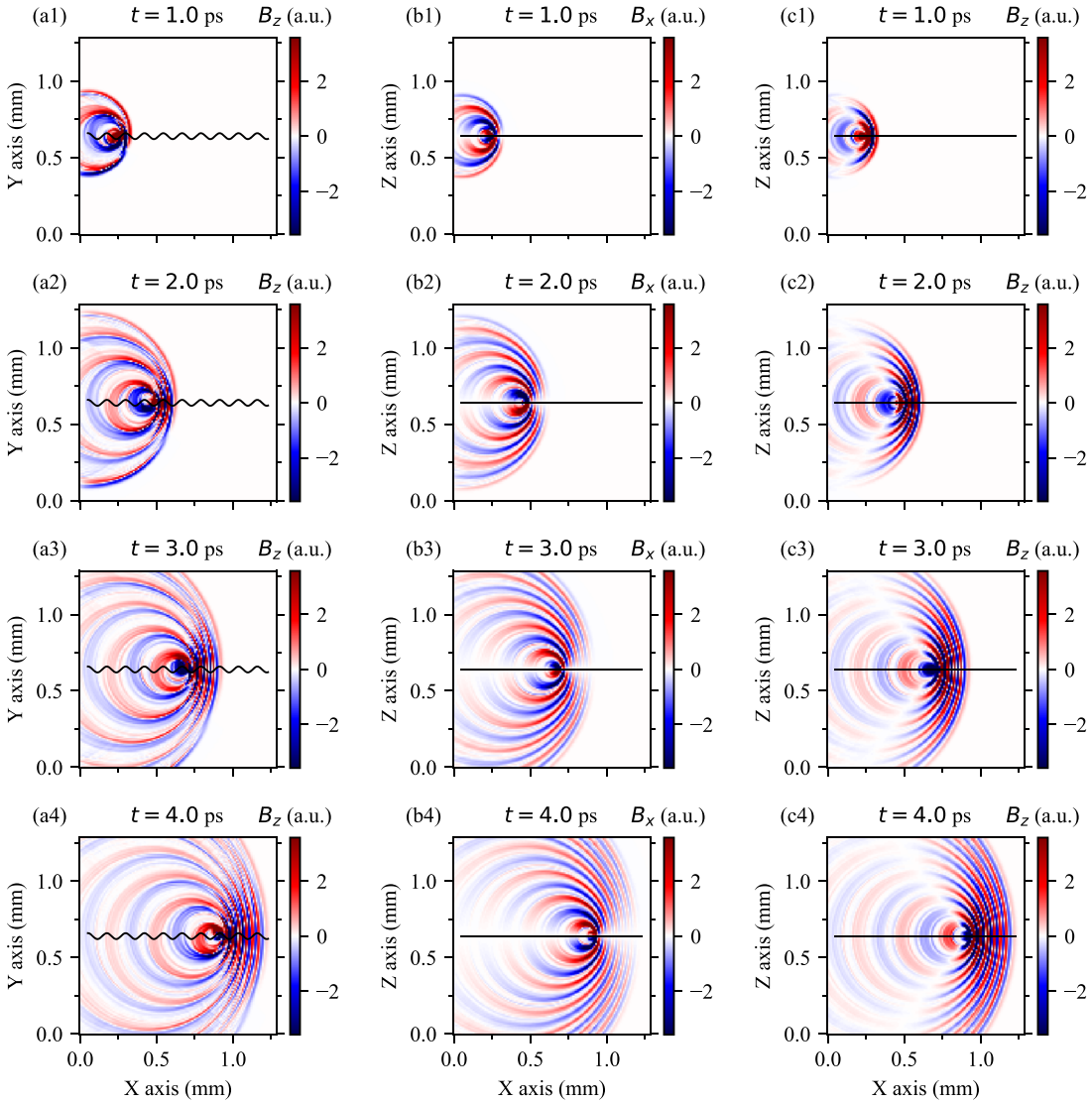

FIG. 3. Electromagnetic fields emitted by the "sine" target with geometry defined by Eq. (1): (a1)–(a4) B_z component in the plane of the target, i.e., at $z = 0.64$ mm, at moments of time 1.0, 2.0, 3.0, and 4.0 ps, respectively; (b1)–(b4) B_x component in the plane $y = 0.64$ mm at the same moments of time; (c1)–(c4) B_z component in the plane $y = 0.64$ mm at the same moments of time. The projections of the target on the considered planes are shown as solid black lines. For clarity of the field profiles, the energy dissipation of the discharge current pulse is not taken into account in these plots.

driver is shorter than the target width[26,27] but is not considered in the present study.

In the modeling performed here, the discharge current pulse was initialized at the left tip of the wire and propagated to the right. Its spatiotemporal profile was taken from a simulation with a straight wire, irradiated by a laser pulse with duration of 50 fs. The results obtained, presented in Fig. 3, show that this oscillating discharge current pulse emits electromagnetic radiation that tears off from the target. Examples of the far-field patterns, obtained on the side planes of the simulation box at $x = 1.28$ mm and $z = 1.28$ mm, are presented in Fig. 4. As can be seen, the radiation has an almost regular periodic nature. As the source moves along the wire, the patterns in Figs. 4(c1)–4(c4) and 4(d1)–4(d4) gradually shift to the right, following, with a delay, the emitting current pulse. For distances greater than the total length of the target, this effect becomes less pronounced.

We next consider radiation emitted by "triangle" and "square" targets. The former was defined as follows:

$$\begin{cases} y = L_y/2 + a_1(1 - 2\arccos[0.99\sin(x/a_2)]/\pi), \\ z = L_z/2, \end{cases} \tag{2}$$

with $a_1 \approx 39\ \mu$m defining the amplitude and $a_2 \approx 8.5\ \mu$m defining the period. The "square" target was defined as follows:

$$\begin{cases} y = L_y/2 + 2a_1\arctan[100\sin(x/a_2)]/\pi, \\ z = L_z/2, \end{cases} \tag{3}$$

with $a_1 \approx 27.5\ \mu$m defining the amplitude and $a_2 \approx 8.5\ \mu$m defining the period. All three targets ("sine," "triangle," and "square") have the same period length 150 μm. The formulas adopted for the targets allow the sharpness of transitions between different half-periods to be controlled by changing the factors preceding $\sin(x/a_2)$. Here, these factors were set to 0.99 and 100 to make transitions smooth enough from the point of view of technical feasibility aiming at experimental realization. The distributions of the electromagnetic

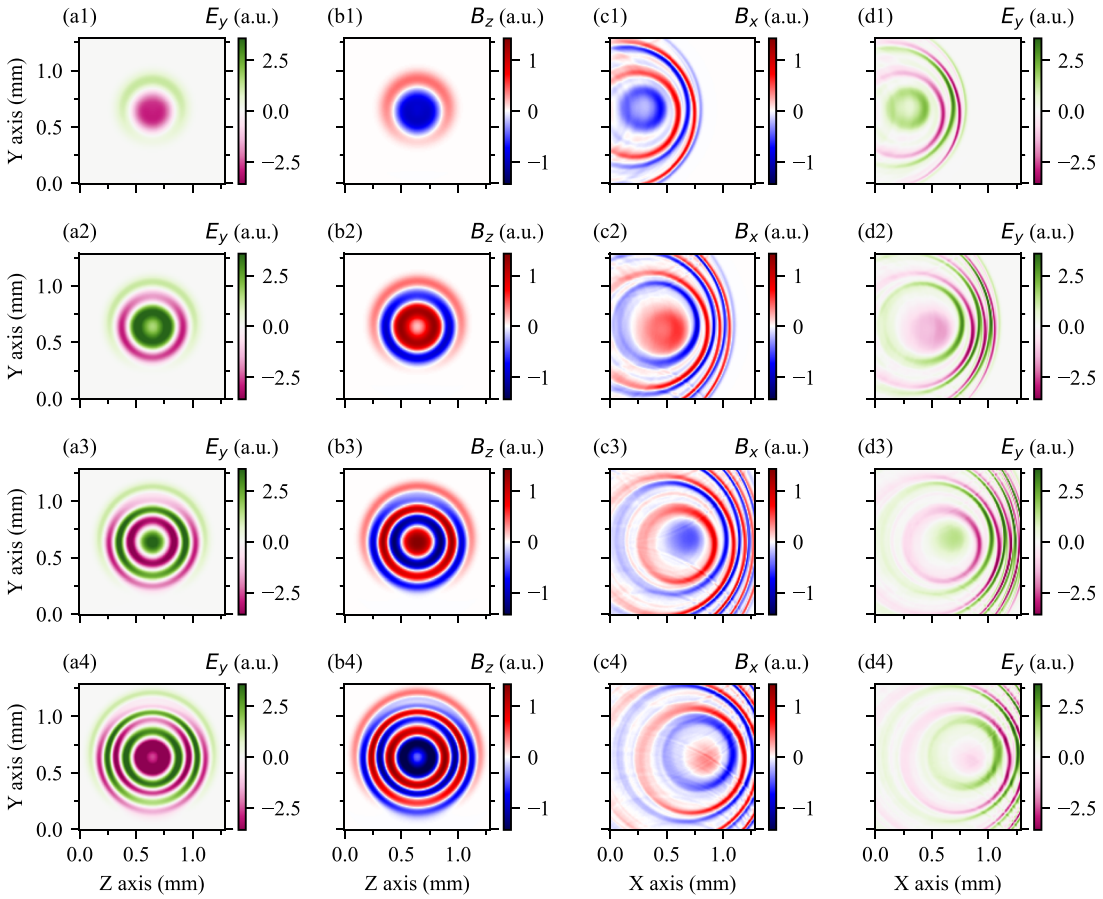

FIG. 4. Electromagnetic fields emitted by the "sine" target with geometry defined by Eq. (1) on the edges of the simulation box: (a1)–(a4) E_y component on the edge $x = 1.28$ mm at moments of time 4.27, 4.37, 4.47, and 4.57 ps, respectively; (b1)–(b4) B_z component on the edge $x = 1.28$ mm at moments of time 4.27, 4.37, 4.47, and 4.57 ps, respectively; (c1)–(c4) B_x component on the edge $z = 1.28$ mm at moments of time 3.4, 4.2, 5.0, and 5.8 ps, respectively; (d1)–(d4) E_y component on the edge $z = 1.28$ mm at moments of time 3.4, 4.2, 5.0, and 5.8 ps, respectively. For clarity of the field profiles, the energy dissipation of the discharge current pulse is not taken into account in these plots.

fields for these two cases are illustrated in Figs. 6(c) and 6(d), and in Figs. S2 and S3 in the supplementary material. The emitted field patterns for the "triangle," and "square" targets are qualitatively similar to the distributions produced by the current oscillating in the "sine" wire. A distinct electromagnetic wave is formed as the current goes along the shaped wires, and it separates from the discharge pulse and propagates independently. For the "triangle" and "square" targets, the separation between the wave front and the discharge current pulse along the x axis is more pronounced than in the case of the "sine" wire defined by Eq. (1). This is a consequence of a lower average propagation velocity along the x axis, since the former two targets have larger travel paths along the y axis. In addition, this leads to a less pronounced Doppler shift for the "triangle" and "square" targets. It should also be noted that the field profiles become more complex than those for the "sine" target. In particular, the waveform shifts from sinusoidal to a more irregular form, while transitions between positive and negative half-periods of the wave become sharper, reflecting sharper changes in the geometry of the wire itself.

IV. DISCUSSION

For all the targets considered, the induced THz radiation has an angular distribution with frequency depending on the direction as a result of a significant Doppler shift due to the high propagation velocity of the discharge $v \sim c$; see Fig. 5(a), where the power spectral density (PSD) is plotted for three different angular directions. For $\theta = 0^\circ$, i.e., along the x axis, the central frequency that corresponds to the peak PSD is about 7 THz. In the opposite direction, the wavelength is stretched, and the central frequency decreases to 1 THz. The energy dissipation with a relatively slow temporal scale as shown in Fig. 2(d) leads to the appearance of a subtle peak in the low-frequency range 0.1–1 THz indicated by the black arrow in Fig. 5(a); its frequency corresponds to the characteristic decay scale $\sim \tau_{\mathrm{dec.}}$. The emission of an angular sweep through distinct spectral bands between both extremes in the forward and backward directions is an outstanding feature of the proposed platform. By collimation to $\theta = 90^\circ$ through the use of an on-axis parabola, a spatial frequency chirp may be obtained in the resulting THz beam. For this, the

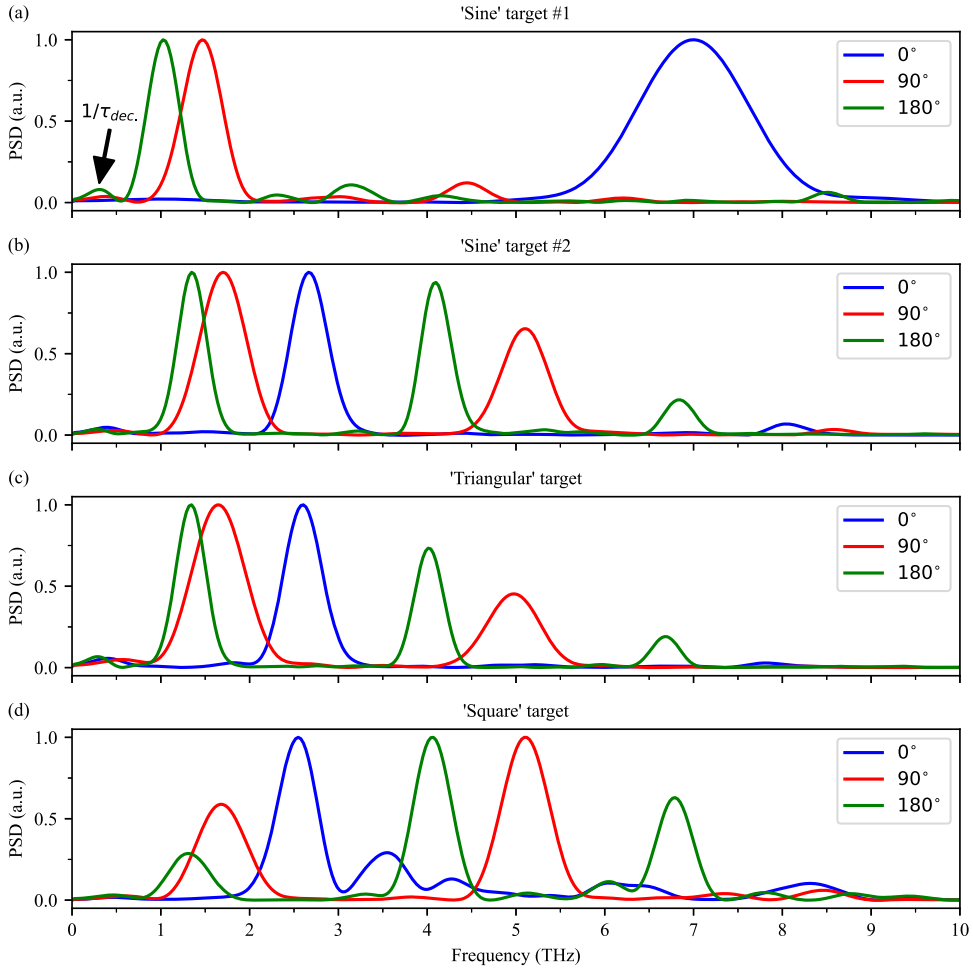

FIG. 5. Power spectral density (PSD) for targets with different geometries: (a) "sine" target with geometry defined by Eq. (1); (b) "sine" target with geometry defined by Eq. (4); (c) "triangle" target with geometry defined by Eq. (2); (d) "square" target with geometry defined by Eq. (3). The blue curves correspond to the PSD in the forward direction, i.e., $\theta = 0^\circ$, the red curves correspond to the PSD in the perpendicular direction, i.e., $\theta = 90^\circ$, and the green curves correspond to the PSD in the backward direction, i.e., $\theta = 180^\circ$. The subtle peak in the region 0.1–1 THz indicated by the black arrow in (a) results from the "slow" decay of the amplitude of the discharge current pulse with characteristic decay time $\tau_{\mathrm{dec.}}$.

parabola has to be placed close enough to the wire, at a distance comparable to its aperture radius, so that it may capture THz radiation in a sufficient solid angle over which the spatial chirp is observed. In practical terms, the spatial chirp can be directly applied in spatially resolved probing schemes or transformed to a temporal chirp using dispersive elements such as gratings.

Also of interest is the direction $\theta = 90°$. To measure the spectrum in this direction in the simulations, points with zero longitudinal field component were selected from the obtained results; for example, distinct $B_z = 0$ lines [see Figs. 3(c1)–3(c4)] and transverse field components (e.g., B_x) were measured at these points to calculate the spectrum along the z-axis direction. The central frequency of the obtained spectrum is ~1.5 THz, which corresponds roughly to the length of one period of a "sine" of ~150 μm, although it is somewhat less. For $a = 20$ μm, the length of one period of a "sine" is $l_0 \approx 150$ μm, and the expected central frequency is $f = v_0/l_0 = 1.8$ THz. The observed slight discrepancy between these frequencies can be explained by the fact that in the simulations, the frequency is extracted in the vicinity of the target from the signal along the cone of the transverse electromagnetic fields; see, for

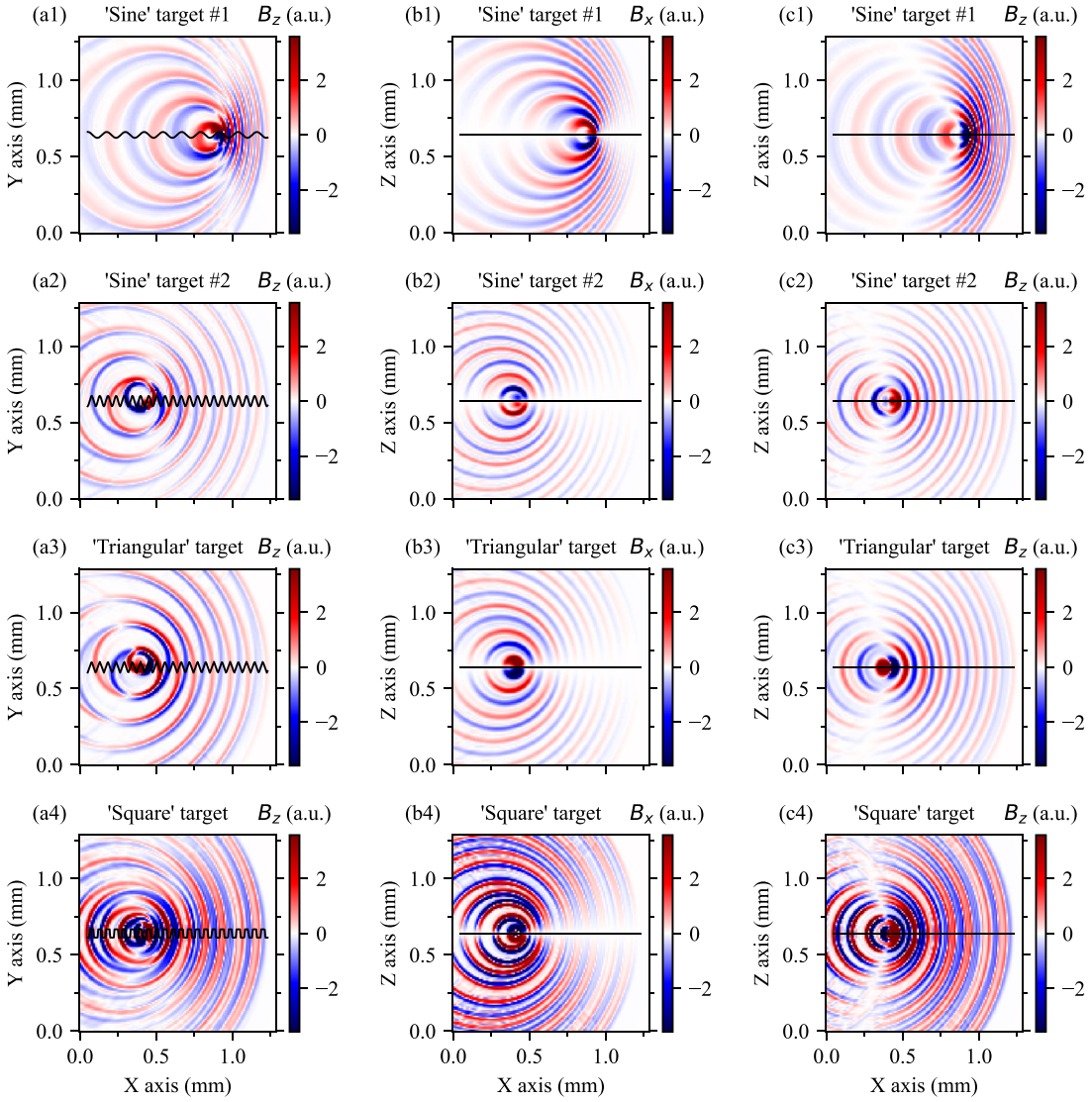

FIG. 6. (a1)–(c1) Electromagnetic fields emitted by the "sine" target with geometry defined by Eq. (1): (a1) B_z component in the plane of the target, i.e., at $z = 0.64$ mm, at 4.0 ps; (b1) B_x component in the plane $y = 0.64$ mm at the same moment of time; (c1) B_z component in the plane $y = 0.64$ mm at the same moment of time. (a2)–(c2) The same, but for the "sine" target with geometry defined by Eq. (4). (a3)–(c3) The same, but for the "triangle" target with geometry defined by Eq. (2). (a4)–(c4) The same, but for the "square" target with geometry defined by Eq. (3). The projections of the targets on the considered planes are shown as solid black lines. For clarity of the field profiles, the energy dissipation of the discharge current pulse is not taken into account in these plots.

example, Figs. 3(c1)–3(c4). It should be noted that for the other targets considered (see Fig. 6), with the same value of l_0 but lower propagation velocity along the x axis and consequently less pronounced source displacement, the main frequency of radiation at $\theta = 90°$ closely corresponds to the geometrically defined value of 1.8 THz; see the red curves in Figs. 5(b)–5(d).

For an explicit comparison, another "sine" target with different ratio of amplitude to period was considered. Its geometry was set as follows:

$$\begin{cases} y = L_y/2 + a_1 \sin(x/a_2), \\ z = L_z/2, \end{cases} \tag{4}$$

where $a_1 \approx 34\ \mu$m defines the amplitude and $a_2 \approx 8.5\ \mu$m defines the period. The overall length of one period along the wire is 150 μm, the same as for the other targets, but in this case the amplitude-to-period ratio is four times greater than that for the target defined by Eq. (1). The immediate consequence of this change is that now the current needs more time for one oscillation. This results in a lower average propagation velocity along the x axis, resulting in a less pronounced Doppler shift. The obtained distributions of electromagnetic fields in the plane of the target and the perpendicular plane are shown in Figs. 6(a2)–6(c2) and in Fig. S1 in the supplementary material. In addition to the reduced Doppler shift, one can see that the spatiotemporal profiles of the emitted fields change. Their spectral characteristics also change dramatically; see Fig. 5(b). For all the examples of wire geometries considered in this study, the ratio of the characteristic undulation amplitude to the undulation period is $a_1 \geq a_2$. In the opposite case, when $a_1 \ll a_2$, the emission efficiency starts to drop, and the field pattern created around the target gradually transitions to a single monopolar field bound to the propagating discharge; see the examples of electromagnetic field distributions for targets with $a_1 \ll a_2$ in Fig. S4 of the supplementary material.

The angular distribution of the radiated power for undulating wires of different shapes is an interesting topic for discussion. Compare two different "sine" targets with $a_1 = a_2 = 20\ \mu$m and with $a_1 = 34\ \mu$m, $a_2 = 8.5\ \mu$m. To analyze the angular distribution of the radiated power, the time-integrated fluence of the Poynting vector through the edge planes of the simulation box was calculated. For this, the target, reduced to the three undulating periods, was located at the center of the simulation box at $(x, y, z) = (0, 0, 0)$, the discharge current pulse duration was ~50 fs, and its amplitude increased linearly from zero to 10^5 A on the first period, remained constant at 10^5 A on the second period, and decreased linearly from 10^5 A to zero on the third period. The calculated fluence was normalized per value emitted on the second period when the current amplitude was constant. The results obtained are presented in Fig. 7. As can be seen from Fig. 7(a), the target with $a_1 = 20\ \mu$m, $a_2 = 20\ \mu$m mostly emits in the forward direction, as a consequence of the high average propagation velocity along the x axis. For the sideward and backward directions, the effective intensity of THz radiation appears to be much less. For the other target, with $a_1 = 34\ \mu$m, $a_2 = 8.5\ \mu$m, the directional patterns of the radiation change substantially. The energy is now redistributed over other edges of the simulation box, and a high fluence can be observed on both the side edge $(z = z_{\min})$ in the forward direction and the lower edge $(y = y_{\min})$ in the sideward direction in the plane of the wire. For the latter, the distribution has a peculiar "C" shape, with a noticeable minimum. These patterns appear as a consequence of the relativistic effects of the discharge propagation; see Fig. S5 in the supplementary material for further details. From the analysis presented here, it follows that the angular distribution of the radiated power is determined by the target geometry. The specifics of the distribution should be taken into account when planning experimental studies and may be important for applications where certain properties of the THz radiation are required.

The results presented here demonstrate that the shape of the target indeed plays a significant role, affecting the angular distribution of emitted power, as shown in Fig. 7, as well as the spatiotemporal profile of the fields emitted by the target and their spectral characteristics, as shown in Figs. 5(c) and 5(d). As the target profile, while retaining its periodic nature, becomes more complex, other frequency components appear in the spectra. These are particularly pronounced for $\theta = 90°$ and $\theta = 180°$, whereas for $\theta = 0°$, most of the radiation is still emitted at one central frequency, as shown by the results for the "square" and "triangle" targets. The main frequency just shifts from 7 to ~2.6 THz as a result of a smaller Doppler shift along the x axis. The frequency properties may be controlled to a wide extent by the geometry of the target to provide either a relatively simple field profile [Figs. 6(a1)–6(c1)] and spectra with one pronounced frequency component in a particular direction [Fig. 5(a)] or more complex profiles [Figs. 6(a2)–6(c2), 6(a3)–6(c3), and 6(a4)–6(c4)] with one or two additional frequencies [Figs. 5(b)–5(d)], depending on the needs of a particular application. It is interesting to note that for the "square" target, the second harmonic for $\theta = 90°$ and $\theta = 180°$ is more pronounced than the fundamental one, which is related to the occurrence of two sharp 90° breaks in one undulation period.

The selection of a frequency band tailored to fit a specific application is possible between the Doppler-shifted maximum and minimum frequencies when selecting a certain slice of emission (e.g., by a donut-shaped aperture). This particularly benefits from a small angular gradient of frequencies. If needed, the frequency range offered by different angular directions can be extended by increasing the velocity and resulting Doppler shift in the x-axis direction and by adjusting the amplitude-to-period ratio of the target.

Although a full analytical consideration of curved targets is complicated, some general relations may be obtained directly in the framework of a simplified model. Consider a δ-function current $J \sim J_0\delta(l - v_0 t)$, where J_0 is the current amplitude, $l = l(x)$ is the current pulse position along the wire, and v_0 is the propagation velocity, which appears from our simulations to be very close to the velocity of light. Where necessary for certain calculations, it is possible to consider, for example, a "sine" wire $y = a \sin \varkappa x$ such that for the first "sine" target (No. 1) $\varkappa a = 1$, and for the second one (No. 2) $\varkappa a = 4$. Then,

$$\mathbf{J} = J_0\delta(l - v_0 t)\left(\frac{dx}{dl}\mathbf{e}_x + \frac{dy}{dl}\mathbf{e}_y\right), \tag{5}$$

and, without approximations, the vector potential is

$$\mathbf{A}(t) = \frac{J_0}{c}\int dl\, \frac{\delta(l - v_0 t')}{|\mathbf{R} - \mathbf{r}|}\left(\frac{dx}{dl}\mathbf{e}_x + \frac{dy}{dl}\mathbf{e}_y\right), \tag{6}$$

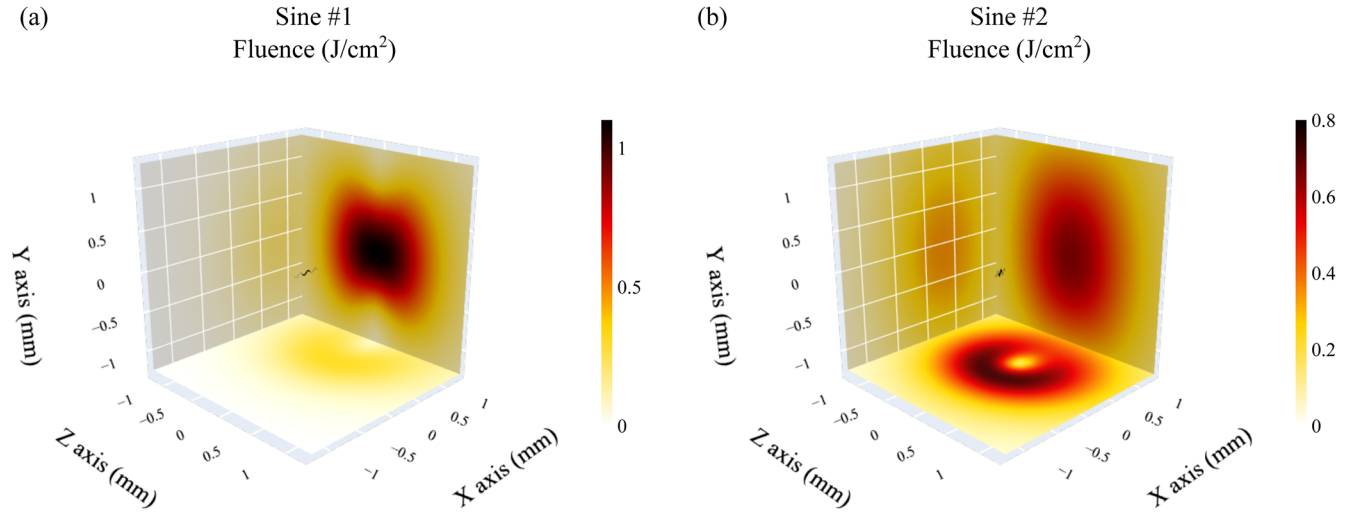

FIG. 7. Time-integrated energy fluence of THz radiation through the edges of the simulation box for three-period sine targets with (a) $a_1 = a_2 = 20\ \mu$m (a) and (b) $a_1 = 34\ \mu$m, $a_2 = 8.5\ \mu$m. The target is located at the center of the simulation box at $(x, y, z) = (0, 0, 0)$. The current pulse duration is ~50 fs, and its amplitude increases linearly from zero to 10^5 A on the first period, stays constant at 10^5 A on the second period, and decreases linearly from 10^5 A to zero on the third period. The fluence is normalized per value emitted on the second period when the current amplitude is constant.

where $t' = t - |\mathbf{R} - \mathbf{r}|/c$ and $\mathbf{R}$ is the vector to the observer. For a given direction $\mathbf{R}$, it is possible to find the polarization of the emitted wave, considering the component of the electric field $\mathbf{E} = -(1/c)\partial\mathbf{A}/\partial t$ normal to $\mathbf{R}$. That is, for $\mathbf{R}\|\mathbf{e}_x$ the wave is y-polarized, for $\mathbf{R}\|\mathbf{e}_y$ the wave is x-polarized, and for $\mathbf{R}\|\mathbf{e}_z$ the polarization is a nontrivial combination of both. For a "sine" wire, the expression (6) may then be rewritten as

$$\mathbf{A}(t) = \frac{J_0}{c}\int dx\,\frac{\delta\big(l(x) - v_0 t'\big)}{|\mathbf{R} - \mathbf{r}(x)|}(\mathbf{e}_x + \mathbf{e}_y \varkappa a\,\cos\,\varkappa x), \tag{7}$$

where

$$l(x) = \frac{\sqrt{a^2\varkappa^2 + 1}}{\varkappa} E\left(\varkappa x, \frac{a^2\varkappa^2}{a^2\varkappa^2 + 1}\right), \tag{8}$$

$E(\xi, k)$ is the elliptic integral of the second kind, and

$$t' = t - \frac{|\mathbf{R} - \mathbf{r}(x)|}{c} \tag{9}$$

is the retarded time.

In the wave zone, it is possible to assume $|\mathbf{R} - \mathbf{r}(x)| \approx R$ in the denominator, and then Eq. (7) gives for the frequency dependence

$$\mathbf{A}(\omega) = \frac{J_0}{cRv_0}\int dx\,\exp\left[i\frac{\omega l(x)}{v_0} - i\frac{\omega\mathbf{R}\cdot\mathbf{r}}{cR} + i\frac{\omega R}{c}\right] \times (\mathbf{e}_x + \mathbf{e}_y \varkappa a\,\cos\,\varkappa x). \tag{10}$$

Using Eq. (10), one can find the characteristic frequencies of the radiation, using, for example, a numerical approach.

For the chosen geometry, a more interesting frequency dependence is expected for $A_y(\omega)$:

$$A_y(\omega) = \frac{J_0 e^{i\omega R/c}}{2cRv_0}\sum_{\pm}\int dx\,\exp\left[i\frac{\omega l(x)}{v_0} - i\frac{\omega\mathbf{R}\cdot\mathbf{r}}{cR} \pm i\varkappa x\right]. \tag{11}$$

For a rough estimate of the main carrier frequency ω_0, the wire length can be rewritten as

$$l(x) = x\sqrt{a^2\varkappa^2 + 1}\,\mathscr{E}\left(\frac{a^2\varkappa^2}{a^2\varkappa^2 + 1}\right) + \mathscr{F}_{\rm osc}(x), \tag{12}$$

where $\mathscr{F}_{\rm osc}(x)$ is the oscillating function with zero average, and $\mathscr{E}(k)$ is the full elliptic integral of the second kind. The estimate of ω_0 comes from the integral in (11) by omitting oscillating terms in the exponent. Then

$$\omega_0 \sim \frac{\varkappa}{\frac{2\sqrt{1+\varkappa^2 a^2}\,\mathscr{E}\left(\frac{a^2\varkappa^2}{a^2\varkappa^2+1}\right)}{\pi v_0} + \frac{\cos\theta}{c}}, \tag{13}$$

where θ is the angle between the observation direction and $\mathbf{e}_x$. This expression can be rewritten in terms of the half-length of a single undulation $l_{1/2}$, which, for the "sine" wire considered here, is given by

$$l_{1/2} = \frac{\sqrt{a^2\varkappa^2 + 1}}{\varkappa}\mathscr{E}\left(\frac{a^2\varkappa^2}{a^2\varkappa^2 + 1}\right), \tag{14}$$

and as a rough, though general, estimate for an arbitrary undulating wire with a characteristic period defined with $\varkappa$, one may use

$$\omega_0 \sim \frac{\varkappa}{\frac{2\varkappa}{\pi v_0} l_{1/2} + \frac{\cos\theta}{c}}. \tag{15}$$

The estimates (13) and (15) work better for radiation propagating parallel to $\mathbf{e}_x$, since the y projection of R is absent. In the limiting case $\varkappa a \to \infty$, both forward and backward $\omega_0 \approx \pi v_0/2a$, which corresponds to a charge that oscillates up and down with amplitude $a/2$ and velocity v_0. In the opposite case, which corresponds to an infinitely stretched wire, $\omega_0 \approx \varkappa(1/v_0 \pm 1/c)^{-1}$, with "−" for the forward and "+" for the backward direction. So, the higher the velocity v_0, the more pronounced is the Doppler shift.

For an arbitrary direction, the estimate (15) is also in good accordance with the simulation results. The dependences of ω on $\varkappa a$ and θ are shown for a propagation velocity of $0.9c$ in Figs. 8(a) and 8(b) and for a propagation velocity of $0.99c$ in Figs. 8(c) and 8(d). The geometrical dependence [see Figs. 8(a) and 8(c)] demonstrates that the frequency increases for small $\varkappa a$ and $\theta = 0$, and the maximum is higher for higher propagation velocity. For the other two angles considered, $\theta = \pi/2$ and $\theta = \pi$, the frequency grows monotonically with $\varkappa a$. For all angles, the asymptotic value corresponds to $\pi v_0/2a$, as discussed above. The angular dependences in Figs. 8(b) and 8(d) have a maximum at $\theta = 0$, which is more pronounced for smaller $\varkappa a$. For smaller propagation velocities, the dependence on

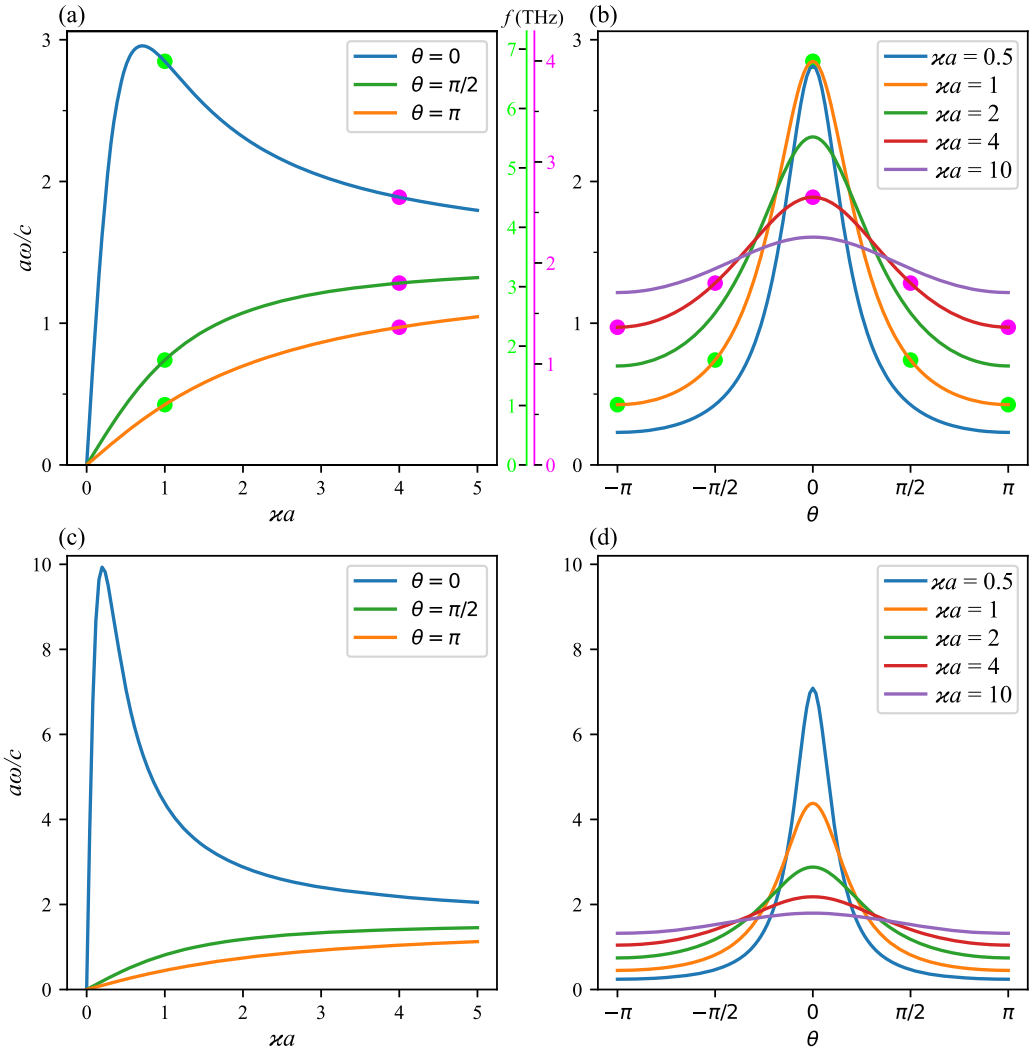

FIG. 8. Results of analytical estimates of the main frequency emitted by the "sine" target: (a) and (c) dependence of the normalized frequency $a\omega/c$ on the geometrical parameter $\varkappa a$ for different directions θ and two different propagation velocities $0.9c$ and $0.99c$, respectively; (b) and (d) dependence of the normalized frequency $a\omega/c$ on the direction θ for different values of the geometrical parameter $\varkappa a$ and two different propagation velocities $0.9c$ and $0.99c$, respectively. The green and magenta filled circles show points corresponding to the geometrical parameters of the sine targets considered in the numerical study, with green and magenta corresponding to the "sine" targets with geometries defined by Eqs. (1) and (4), respectively; their absolute frequency values are marked on the axes with the corresponding color.

$\varkappa a$ is less pronounced than for higher ones, as can be seen from a comparison between Figs. 8(b) and 8(d).

In Figs. 8(a) and 8(b), the green and magenta filled circles correspond to different geometrical parameters in the numerical simulations. The corresponding dimensional frequencies are shown on the additional scales between the panels. Comparison with the spectra shown in Figs. 5(a) and 5(b) demonstrates good quantitative agreement of the main frequencies. The greatest difference is seen for the "sine" target No. 1 at $\theta = \pi/2$. This is partly related to the omission of the oscillating terms mentioned above.

The simple approach presented above also enables one to obtain a qualitative understanding of some effects of a finite current pulse length and its decay rate. The finite length may be modeled using, for example, the Gaussian representation of the delta function $\delta(l(x) - v_0 t) \to \text{Const.} \times \exp\{-\alpha^2[l(x) - v_0 t]^2\}$, with a finite α. Assuming a small current pulse width $\alpha \gg 1$, one obtains a similar result for the spectrum, but with an additional decay $\sim \exp(-\omega^2/\alpha^2 v_0^2)$, which means that the higher frequencies are being cut. Indeed, a smooth long current should not effectively generate frequencies above its inverse characteristic time, which is the current length related to its propagation velocity, and, in the limit, for a constant current, the radiation frequency goes to zero; for a demonstration, see Fig. S6 in the supplementary material. Adding $e^{-\gamma l(x)}$, which imitates the longitudinal decay of the current pulse, to Eq. (6) and so to Eq. (11) would result in an additional imaginary term in Eq. (13), meaning qualitatively a temporal decay and the related widening of the carrier frequency $\Delta\omega/\omega \sim 2\gamma l_{1/2}/\pi$.

It should be noted that the propagation velocity v_0 is usually very close to the velocity of light. This precludes the use of the dipole approximation for calculating the radiation parameters. Actually, the dipole approximation would require omission of all terms with $1/c$ near the other terms with $1/v_0$. That would eliminate, for example, the frequency dependence on the radiation direction [see Eq. (13)], which is one of the most prominent features of the observed effect, as seen in Figs. 3–6.

The amplitude of the electromagnetic fields in the wave zone (i.e., in our case, on the edge planes of the simulation box) depends on the value of the electric current induced in the wire, which in turn is determined by the intensity of the laser driver. The obtained scaling [see Fig. 2(b)] enables estimation of the electric current and consequently the magnitudes of the electromagnetic waves emitted by this current for various intensities of the incident laser pulse. The results are summarized in Table I. Electric fields are extrapolated at a distance of 1 cm, which is reasonable for practical applications, under the assumption that the fields fall off as $1/r$ with distance. The radiated power and the energy are estimated from the obtained electromagnetic field distributions, with account taken of the angular distribution of the radiated energy density. The values of the radiated power and the energy correspond to the first cycle, when the discharge current amplitude is the highest. For the subsequent cycles, they decrease according to the discharge pulse decay law.

For the intensities of 10^{21} W/cm^2 (i.e., 30 J) typical of modern petawatt-class laser systems, the extreme power level of 0.2 TW is generated in the first cycle. In terms of the radiated power, the discussed THz source is not inferior to other schemes based on intense laser–target interaction.[41] The features that make the proposed mechanism distinct, and perhaps more attractive for certain applications, include the possibility of straightforward control of the spectral properties of the THz radiation and its angular distribution with the geometry of the curved wire, the potential for obtaining multiple-cycle THz pulses if the decay scale of the discharge current is smaller that the length of one undulating period of the target, the angular dependence of the spectrum, and the possibility of employing it to obtain THz radiation with a spatial or temporal chirp. In combination with modern femtosecond petawatt laser facilities with achievable repetition rates of up to one shot per minute and peak laser beam powers of up to 10 PW,[42] the discussed mechanism holds great potential for applications that demand a compact spectrally tunable source of intense THz radiation. In addition, for table-top laser systems, the THz output can be further increased by optimization of the interaction conditions, such as by irradiation at grazing incidence or by embedding some micro-structure on the surface of the wire tip to increase the absorption of laser energy and its conversion into the energy of the discharge pulse.

TABLE I. Summary of the properties of produced THz radiation: peak amplitude of electric field, peak radiated power, and full radiated energy for various intensities of the laser pulse driving different initial electric currents J_0 inside a wire. Electric current amplitudes are given for a propagation distance of ~20 μm from the interaction point, and electric fields are extrapolated at a distance of 1 cm. The radiated power and the full radiated energy are calculated with the dissipation of the discharge current pulse taken into account according to the rough and probably excessive estimate based on the simulation for a thin wire; see Fig. 2(d).

$I_{las.}$ (W/cm^2)	J_0 (A)	E_{THz} (V/m)	P_{THz} (W)	U_{THz} (J)
2×10^{19}	1.7×10^4	9×10^7	2×10^9	1.2×10^{-3}
10^{20}	4×10^4	2×10^8	1.3×10^{10}	6×10^{-3}
10^{21}	1.6×10^5	8×10^8	2×10^{11}	0.10
10^{22}	6×10^5	3×10^9	3×10^{12}	1.5
10^{23}	2×10^6	1.0×10^{10}	3×10^{13}	16

An important question is what parameters of the laser pulse are suitable for the excitation of the compact discharge pulses and the subsequent controlled THz emission. To clarify this point, simulations were performed for sub-picosecond laser pulse durations of 0.125–0.50 ps, which are about ten times longer than the femtosecond laser pulses initially considered. It was verified that electromagnetic waves in the THz frequency range can be produced with sub-picosecond laser pulses as well, but their amplitude stays the same as in the case of femtosecond laser pulses or becomes lower (and even much lower in certain directions); see Fig. S6 in the supplementary material for further insight. The reason for the observed decrease in THz emission is that in this case the duration of the discharge current pulses increases to a value at which they start to occupy the full length of an undulation period of the target, thereby impeding the production of electromagnetic radiation. In this regard, it should also be noted that driving the current pulse with the same amplitude and about ten times longer duration to achieve the same intensity of THz radiation requires about ten times more invested laser energy, which shows the advantages of short laser pulses in the considered scheme.

Another issue that is important in the context of the applicability of the proposed scheme is the energy decay of the discharge pulse due to emission of electromagnetic waves, electron heating, and other processes of dissipation. Energy decay due to emission may be estimated using the values from Table I. Suppose a discharge

pulse is produced by tight focusing of a 10 J laser pulse with duration of 30 fs on the shaped target, so that the peak intensity on its surface is about 10^{21} W/cm^2. Assuming 5%–10% of the laser energy is initially converted into the discharge wave, and 70 mJ is emitted on the first cycle, we obtain a conversion efficiency of the discharge pulse energy to emitted electromagnetic waves of about 2%–5% in each period. In this case, it would require at least tens of cycles to fully exhaust the discharge pulse energy with only the radiation. In addition to emission, other processes of dissipation may play a significant role in the decay of the discharge wave.

The presented simulation results for a thin wire [see Fig. 2(d)] probably overestimate the absorption rate, as discussed in Sec. II. In addition, it should be noted that the effect of a wire-guided motion of electrons has been experimentally observed over distances of up to 1 m.[43,44] Already for the rough and probably excessive estimate of the discharge decay rate deduced from the simulation for the thin wire, the energetic efficiency of the laser-to-THz conversion in the considered setup may reach ~1% with multiple-cycle THz radiation. For example, a target designed to emit in the sideward direction at a main frequency of 2 THz has an undulating period of ~150 μm, and even for a decay rate of the order of 250 μm^{-1}, the discharge pulse would travel approximately three full periods before its amplitude decreased by a factor of $1/e^2$. However, as mentioned above, there is experimental evidence that indicates a much smaller decay rate. In this case, and if necessary, the use of targets with smaller undulation periods of a few tens of micrometers may enable the duration of the produced THz pulses to be increased up to $\gtrsim$10 periods and the conversion efficiency to be increased sufficiently beyond 1%–2%.

Finally, it should be noted that an important feature of the setup considered here is its simplicity. Production of the proposed target sizes is feasible with lithographic methods or even by laser cutting; see, for example, Ref. 38, where a 20 μm-thick coil-shaped wire was produced for an experimental study by laser cutting from 20 μm-thick copper foil. The target wire thickness is similar to the usual size of a tightly focused high-power laser spot, and most systems are able to provide sufficiently good pointing stability. Note however, that here idealized wires were considered; in practice, formation and propagation of discharge pulses may depend on the wire quality, which will be studied elsewhere.

V. CONCLUSION

In conclusion, we have demonstrated the possibility of creating short discharge current pulses in extended wire targets irradiated by intense femtosecond laser pulses over a wide range of laser intensities. The proposed approach is based on robust excitation of relativistic discharge pulses under intense laser–matter interaction and may be easily realized. The parameters of the discharge pulses, such as their amplitude and duration, can be controlled by the relevant parameters of the laser driver, namely, its peak intensity and duration. Forcing a laser-induced discharge pulse to oscillate as it travels along the wire by the choice of a specific target geometry turns the target into an antenna that can efficiently emit electromagnetic radiation in the THz range. The angular distribution of the radiated power and the frequency spectrum of the THz radiation obtained in such a way depend on direction and are determined by the target shape. By adjusting the latter according to the requirements of a given application, either simple spectral distributions with a single pronounced frequency defined by the characteristic undulation period of the target or more complex profiles with a few additional frequency components may be obtained in the desired direction. According to estimates based on numerical simulations, the total power emitted in the THz range for laser pulses with intensities $\geq 10^{22}$ W/cm^2 extends at its peak to the terawatt range, and the total radiated energy exceeds a few joules. Such unprecedentedly high THz output coupled with the possibility of controlling its spectral properties opens a pathway to the use of the proposed THz source scheme in numerous applications requiring intense widely controlled THz radiation.

SUPPLEMENTARY MATERIAL

See the supplementary material for more insight about the temporal evolution of the electromagnetic fields emitted by the studied targets of various shapes.

ACKNOWLEDGMENTS

The authors thank Dr. M. Ehret for fruitful discussions of questions related to this work. This work was supported by the Ministry of Science and Higher Education of the Russian Federation (Agreement No. 075-15-2021-1361). We acknowledge the NRNU MEPhI High-Performance Computing Center and the Joint Supercomputer Center RAS.

AUTHOR DECLARATIONS

Conflict of Interest

The authors have no conflicts to disclose.

Author Contributions

N. Bukharskii: Conceptualization (equal); Data curation (equal); Investigation (equal); Methodology (equal); Project administration (equal); Visualization (lead); Writing – original draft (equal). **Ph. Korneev**: Conceptualization (equal); Data curation (supporting); Formal analysis (lead); Funding acquisition (lead); Investigation (equal); Methodology (equal); Project administration (equal); Supervision (lead); Writing – original draft (equal); Writing – review & editing (lead).

DATA AVAILABILITY

The data that support the findings of this study are available from the corresponding author upon reasonable request.

REFERENCES

[1]M. Tonouchi, "Cutting-edge terahertz technology," Nat. Photonics **1**, 97–105 (2007).

[2]S. S. Dhillon, M. S. Vitiello, E. H. Linfield, A. G. Davies, M. C. Hoffmann, J. Booske, C. Paoloni, M. Gensch, P. Weightman, G. P. Williams, E. Castro-Camus, D. R. S. Cumming, F. Simoens, I. Escorcia-Carranza, J. Grant, S. Lucyszyn,

M. Kuwata-Gonokami, K. Konishi, M. Koch, C. A. Schmuttenmaer, T. L. Cocker, R. Huber, A. G. Markelz, Z. D. Taylor, V. P. Wallace, J. Axel Zeitler, J. Sibik, T. M. Korter, B. Ellison, S. Rea, P. Goldsmith, K. B. Cooper, R. Appleby, D. Pardo, P. G. Huggard, V. Krozer, H. Shams, M. Fice, C. Renaud, A. Seeds, A. Stöhr, M. Naftaly, N. Ridler, R. Clarke, J. E. Cunningham, and M. B. Johnston, "The 2017 terahertz science and technology roadmap," J. Phys. D: Appl. Phys. **50**, 043001 (2017).

[3]D. M. Mittleman, "Perspective: Terahertz science and technology," J. Appl. Phys. **122**, 230901 (2017).

[4]T. Amini, F. Jahangiri, Z. Ameri, and M. A. Hemmatian, "A review of feasible applications of THz waves in medical diagnostics and treatments," J. Lasers Med. Sci. **12**, e92 (2021).

[5]A. I. Nikitkina, P. Y. Bikmulina, E. R. Gafarova, N. V. Kosheleva, Y. M. Efremov, E. A. Bezrukov, D. V. Butnaru, I. N. Dolganova, N. V. Chernomyrdin, O. P. Cherkasova, A. A. Gavdush, and P. S. Timashev, "Terahertz radiation and the skin: A review," J. Biomed. Opt. **26**, 043005 (2021).

[6]S. M. Kim, F. Hatami, J. S. Harris, A. W. Kurian, J. Ford, D. King, G. Scalari, M. Giovannini, N. Hoyler, J. Faist, and G. Harris, "Biomedical terahertz imaging with a quantum cascade laser," Appl. Phys. Lett. **88**, 153903 (2006).

[7]C. Yu, S. Fan, Y. Sun, and E. Pickwell-Macpherson, "The potential of terahertz imaging for cancer diagnosis: A review of investigations to date," Quant. Imaging Med. Surg. **2**, 33–45 (2012).

[8]*Terahertz Biomedical Science and Technology*, 0th ed., edited by J.-H. Son (CRC Press, 2014).

[9]Y. Peng, C. Shi, X. Wu, Y. Zhu, and S. Zhuang, "Terahertz imaging and spectroscopy in cancer diagnostics: A technical review," BME Front. **2020**, 2547609.

[10]Z. Vafapour, A. Keshavarz, and H. Ghahraloud, "The potential of terahertz sensing for cancer diagnosis," Heliyon **6**, e05623 (2020).

[11]H. Lindley-Hatcher, R. I. Stantchev, X. Chen, A. I. Hernandez-Serrano, J. Hardwicke, and E. Pickwell-MacPherson, "Real time THz imaging—Opportunities and challenges for skin cancer detection," Appl. Phys. Lett. **118**, 230501 (2021).

[12]H. Cheon, H.-j. Yang, S.-H. Lee, Y. A. Kim, and J.-H. Son, "Terahertz molecular resonance of cancer DNA," Sci. Rep. **6**, 37103 (2016).

[13]H. Cheon, H.-J. Yang, M. Choi, and J.-H. Son, "Effective demethylation of melanoma cells using terahertz radiation," Biomed. Opt. Express **10**, 4931 (2019).

[14]J.-H. Son, S. J. Oh, and H. Cheon, "Potential clinical applications of terahertz radiation," J. Appl. Phys. **125**, 190901 (2019).

[15]J.-H. Son and H. Cheon, "Toward cancer treatment using terahertz radiation: Demethylation of cancer cells," Proc. SPIE **11390**, 1139002 (2020).

[16]K. Kawase, Y. Ogawa, Y. Watanabe, and H. Inoue, "Non-destructive terahertz imaging of illicit drugs using spectral fingerprints," Opt. Express **11**, 2549–2554 (2003).

[17]A. W. M. Lee, B. S. Williams, S. Kumar, Q. Hu, and J. L. Reno, "Real-time imaging using a 4.3-THz quantum cascade laser and a 320/spl times/240 microbolometer focal-plane array," IEEE Photonics Technol. Lett. **18**, 1415–1417 (2006).

[18]D. M. Mittleman, R. H. Jacobsen, and M. C. Nuss, "T-ray imaging," IEEE J. Sel. Top. Quantum Electron. **2**, 679–692 (1996).

[19]H. Zhong, J. Xu, X. Xie, T. Yuan, R. Reightler, E. Madaras, and X.-C. Zhang, "Nondestructive defect identification with terahertz time-of-flight tomography," IEEE Sens. J. **5**, 203–208 (2005).

[20]P. Salén, M. Basini, S. Bonetti, J. Hebling, M. Krasilnikov, A. Y. Nikitin, G. Shamuilov, Z. Tibai, V. Zhaunerchyk, and V. Goryashko, "Matter manipulation with extreme terahertz light: Progress in the enabling THz technology," Phys. Rep. **836–837**, 1–74 (2019).

[21]J. Federici and L. Moeller, "Review of terahertz and subterahertz wireless communications," J. Appl. Phys. **107**, 111101 (2010).

[22]T. Kleine-Ostmann and T. Nagatsuma, "A review on terahertz communications research," J. Infrared, Millimeter, Terahertz Waves **32**, 143–171 (2011).

[23]Y. Zhang, K. Li, and H. Zhao, "Intense terahertz radiation: Generation and application," Front. Optoelectron. **14**, 4–36 (2021).

[24]G.-Q. Liao and Y.-T. Li, "Review of intense terahertz radiation from relativistic laser-produced plasmas," IEEE Trans. Plasma Sci. **47**, 3002–3008 (2019).

[25]S. Tokita, S. Sakabe, T. Nagashima, M. Hashida, and S. Inoue, "Strong subterahertz surface waves generated on a metal wire by high-intensity laser pulses," Sci. Rep. **5**, 8268 (2015).

[26]Y. Tian, J. Liu, Y. Bai, S. Zhou, H. Sun, W. Liu, J. Zhao, R. Li, and Z. Xu, "Femtosecond-laser-driven wire-guided helical undulator for intense terahertz radiation," Nat. Photonics **11**, 242–246 (2017).

[27]K. Nakajima, "Novel efficient THz undulator using a laser-driven wire," Light: Sci. Appl. **6**, e17063 (2017).

[28]K. Teramoto, S. Tokita, T. Terao, S. Inoue, R. Yasuhara, T. Nagashima, S. Kojima, J. Kawanaka, K. Mori, M. Hashida, and S. Sakabe, "Half-cycle terahertz surface waves with MV/cm field strengths generated on metal wires," Appl. Phys. Lett. **113**, 051101 (2018).

[29]Y. Zeng, C. Zhou, L. Song, X. Lu, Z. Li, Y. Ding, Y. Bai, Y. Xu, Y. Leng, Y. Tian, J. Liu, R. Li, and Z. Xu, "Guiding and emission of milijoule single-cycle THz pulse from laser-driven wire-like targets," Opt. Express **28**, 15258–15267 (2020).

[30]D. Zhang, Y. Zeng, Y. Bai, Z. Li, Y. Tian, and R. Li, "Coherent surface plasmon polariton amplification via free-electron pumping," Nature **611**, 55–60 (2022).

[31]D. Zhang, Y. Bai, Y. Zeng, Y. Ding, Z. Li, C. Zhou, Y. Leng, L. Song, Y. Tian, and R. Li, "Towards high-repetition-rate intense terahertz source with metal wire-based plasma," IEEE Photonics J. **14**, 5910605 (2022).

[32]H. B. Zhuo, S. J. Zhang, X. H. Li, H. Y. Zhou, X. Z. Li, D. B. Zou, M. Y. Yu, H. C. Wu, Z. M. Sheng, and C. T. Zhou, "Terahertz generation from laser-driven ultrafast current propagation along a wire target," Phys. Rev. E **95**, 013201 (2017).

[33]Z.-c. Li and J. Zheng, "Terahertz radiation from a wire target irradiated by an ultra-intense laser pulse," Phys. Plasmas **14**, 054505 (2007).

[34]K. Quinn, P. A. Wilson, C. A. Cecchetti, B. Ramakrishna, L. Romagnani, G. Sarri, L. Lancia, J. Fuchs, A. Pipahl, T. Toncian, O. Willi, R. J. Clarke, D. Neely, M. Notley, P. Gallegos, D. C. Carroll, M. N. Quinn, X. H. Yuan, P. McKenna, T. V. Liseykina, A. Macchi, and M. Borghesi, "Laser-driven ultrafast field propagation on solid surfaces," Phys. Rev. Lett. **102**, 194801 (2009).

[35]N. Bukharskii, I. Kochetkov, and P. Korneev, "Terahertz annular antenna driven with a short intense laser pulse," Appl. Phys. Lett. **120**, 014102 (2022).

[36]M. Ehret, M. Bailly-Grandvaux, P. Korneev, J. I. Apiñaniz, C. Brabetz, A. Morace, P. Bradford, E. d'Humières, G. Schaumann, V. Bagnoud, S. Malko, K. Matveevskii, M. Roth, L. Volpe, N. C. Woolsey, and J. J. Santos, "Guided electromagnetic discharge pulses driven by short intense laser pulses: Characterization and modeling," Phys. Plasmas **30**, 013105 (2023).

[37]P. Korneev, E. d'Humières, and V. Tikhonchuk, "Gigagauss-scale quasistatic magnetic field generation in a snail-shaped target," Phys. Rev. E **91**, 043107 (2015); arXiv:1410.0053.

[38]I. V. Kochetkov, N. D. Bukharskii, M. Ehret, Y. Abe, K. F. F. Law, V. Ospina-Bohorquez, J. J. Santos, S. Fujioka, G. Schaumann, B. Zielbauer, A. Kuznetsov, and P. Korneev, "Neural network analysis of quasistationary magnetic fields in microcoils driven by short laser pulses," Sci. Rep. **12**, 13734 (2022).

[39]J. Derouillat, A. Beck, F. Pérez, T. Vinci, M. Chiaramello, A. Grassi, M. Flé, G. Bouchard, I. Plotnikov, N. Aunai, J. Dargent, C. Riconda, and M. Grech, "Smilei: A collaborative, open-source, multi-purpose particle-in-cell code for plasma simulation," Comput. Phys. Commun. **222**, 351–373 (2018).

[40]A. V. Brantov, A. S. Kuratov, Y. M. Aliev, and V. Y. Bychenkov, "Ultrafast target charging due to polarization triggered by laser-accelerated electrons," Phys. Rev. E **102**, 021202 (2020); arXiv:2002.07436.

[41]G.-Q. Liao, H. Liu, G. G. Scott, Y.-H. Zhang, B.-J. Zhu, Z. Zhang, Y.-T. Li, C. Armstrong, E. Zemaityte, P. Bradford, D. R. Rusby, D. Neely, P. G. Huggard, P. McKenna, C. M. Brenner, N. C. Woolsey, W.-M. Wang, Z.-M. Sheng, and

J. Zhang, "Towards terawatt-scale spectrally tunable terahertz pulses via relativistic laser-foil interactions," Phys. Rev. X **10**, 031062 (2020).
[42]F. Lureau, G. Matras, O. Chalus, C. Derycke, T. Morbieu, C. Radier, O. Casagrande, S. Laux, S. Ricaud, G. Rey *et al.*, "High-energy hybrid femtosecond laser system demonstrating 2 × 10 PW capability," High Power Laser Sci. Eng. **8**, e43 (2020).
[43]S. Tokita, K. Otani, T. Nishoji, S. Inoue, M. Hashida, and S. Sakabe, "Collimated fast electron emission from long wires irradiated by intense femtosecond laser pulses," Phys. Rev. Lett. **106**, 255001 (2011).
[44]H. Nakajima, S. Tokita, S. Inoue, M. Hashida, and S. Sakabe, "Divergence-free transport of laser-produced fast electrons along a meter-long wire target," Phys. Rev. Lett. **110**, 155001 (2013).